Quantitative imaging of nanoscale mechanical properties using hybrid nanoindentation and force modulation

S. A. Syed Asif
Department of Materials Science, University of Florida, Gainesville, Florida 32611

K. J. Wahl[a] and R. J. Colton
Naval Research Laboratory, Code 6170, Washington, DC 20375

O. L. Warren
Hysitron Incorporated, Minneapolis, Minnesota 55439

In this article, we present a quantitative stiffness imaging technique and demonstrate its use to directly map the dynamic mechanical properties of materials with nanometer-scale lateral resolution. For the experiments, we use a "hybrid" nanoindenter, coupling depth-sensing nanoindentation with scanning probe imaging capabilities. Force modulation electronics have been added, enhancing instrument sensitivity and enabling measurements of time dependent materials properties (e.g., loss modulus and damping coefficient) not readily obtained with quasi-static indentation techniques. Tip–sample interaction stiffness images are acquired by superimposing a sinusoidal force ($\sim$1 μN) onto the quasi-static imaging force (1.5–2 μN), and recording the displacement amplitude and phase as the surface is scanned. Combining a dynamic model of the indenter (having known mass, damping coefficient, spring stiffness, resonance frequency, and modulation frequency) with the response of the tip–surface interaction, creates maps of complex stiffness. We demonstrate the use of this approach to obtain quantitative storage and loss stiffness images of a fiber-epoxy composite, as well as directly determine the loss and storage moduli from the images using Hertzian contact mechanics. Moduli differences as small as 20% were resolved in the images at loads two orders of magnitude lower than with indentation, and were consistent with measurements made using conventional quasi-static depth-sensing indentation techniques. © *2001 American Institute of Physics.* [DOI: 10.1063/1.1380218]

I. INTRODUCTION

The objective of the present work is to map mechanical properties quantitatively over an area on a sample surface. In the mechanics community, a traditional approach involves the use of indentation arrays to construct hardness and modulus maps.[1,2] However, for quantitative and meaningful measurements, the indents have to be finitely spaced and thousands of indents have to be performed to obtain even a rudimentary map; this is time consuming and lateral resolution is limited by the indent spacing.

Mechanical property mapping can be significantly enhanced by the addition of tip–sample rastering technology (through piezoelectric scanners), enabling much finer tip–sample positioning below the optical limit. With cantilever-based atomic force microscopy (AFM), maps of adhesion[3–5] and elastic properties[6,7] can be obtained through multiple individual force–distance curves. Resolution is again limited by contact area if the tip–sample interaction is elastic, or by appropriate spacing if the deformation is plastic. Quantitative analyses of AFM data are complicated by problems relating to tip deformation and geometry, piezo hysteresis and creep, as well as an off-normal tip approach.[8–10]

More recently, numerous AFM imaging techniques employing modulation have been developed. In these techniques, the changes in amplitude or phase response of an oscillating tip or sample as the tip is scanned over a heterogeneous sample can be used to map materials property variations. Most of these techniques utilize displacement modulation, where either the tip holder or sample is oscillated, and the tip–sample response (amplitude or phase shift) used to provide an image.[11–17] In these techniques, the tip can be either in continuous or intermittent contact with the sample.

While these configurations are powerful imaging tools, quantitative interpretation of the data requires knowledge of often complicated system dynamics.[18] Coupled with the complex nature of the tip–sample interaction (especially with intermittent contact modes), the resulting data are difficult to model and often misinterpreted. For example, phase shifts observed in one form of intermittent contact mode imaging ("tapping mode") are necessarily due to energy dissipation (damping and adhesion);[19,20] These dissipative processes are often ignored and the phase response incorrectly ascribed purely to elasticity variations. Hence, while imaging "elasticity" is possible, quantification is nontrivial. Furthermore, the inherent problems associated with vibrating cantilevers (e.g., bistabilities[21] and multiple resonances), unknown electronics corrections, and feedback issues make quantitative interpretation of image data extremely difficult.[22,23]

a)Electronic mail: wahl@stm2.nrl.navy.mil

Report Documentation Page

Public reporting burden for the collection of information is estimated to average 1 hour per response, including the time for reviewing instructions, searching existing data sources, gathering and maintaining the data needed, and completing and reviewing the collection of information. Send comments regarding this burden estimate or any other aspect of this collection of information, including suggestions for reducing this burden, to Washington Headquarters Services, Directorate for Information Operations and Reports, 1215 Jefferson Davis Highway, Suite 1204, Arlington VA 22202-4302. Respondents should be aware that notwithstanding any other provision of law, no person shall be subject to a penalty for failing to comply with a collection of information if it does not display a currently valid OMB control number.

1. REPORT DATE **2001**	2. REPORT TYPE	3. DATES COVERED **00-00-2001 to 00-00-2001**

4. TITLE AND SUBTITLE	5a. CONTRACT NUMBER
Quantitative imaging of nanoscale mechanical properties using hybrid nanoindentation and force modulation	5b. GRANT NUMBER
	5c. PROGRAM ELEMENT NUMBER
6. AUTHOR(S)	5d. PROJECT NUMBER
	5e. TASK NUMBER
	5f. WORK UNIT NUMBER

7. PERFORMING ORGANIZATION NAME(S) AND ADDRESS(ES) **Naval Research Laboratory,Code 6170,4555 Overlook Avenue, SW,Washington,DC,20375**	8. PERFORMING ORGANIZATION REPORT NUMBER

9. SPONSORING/MONITORING AGENCY NAME(S) AND ADDRESS(ES)	10. SPONSOR/MONITOR'S ACRONYM(S)
	11. SPONSOR/MONITOR'S REPORT NUMBER(S)

12. DISTRIBUTION/AVAILABILITY STATEMENT
Approved for public release; distribution unlimited

13. SUPPLEMENTARY NOTES

14. ABSTRACT

15. SUBJECT TERMS

16. SECURITY CLASSIFICATION OF:			17. LIMITATION OF ABSTRACT	18. NUMBER OF PAGES **9**	19a. NAME OF RESPONSIBLE PERSON
a. REPORT **unclassified**	b. ABSTRACT **unclassified**	c. THIS PAGE **unclassified**			

Like normal modulation techniques (e.g., perpendicular to sample normal), lateral modulation of the sample in the AFM can be used to map sample inhomogeneities like defects[12] or friction contrast,[24] as well as glass transition temperatures.[25] If great care is taken, quantitative stiffness images can be obtained;[26] however, potential frictional contributions due to slip, as well as cantilever issues (e.g., matching cantilever and sample stiffnesses, and lateral force calibration difficulties) limit the technique.

Force modulation methods, where a force (rather than displacement) is applied directly to the tip, have been used in indentation to enhance sensitivity. If the dynamic response of the indenter is well calibrated and modeled, dynamic mechanical properties (e.g., storage and loss moduli) can be measured.[27,28] Force modulation is also possible in AFM,[29,30] which gives far greater sample positioning and added imaging capabilities compared to conventional nanoindenters. However, the small forces applied in AFM limit the range of samples that can be studied.

The sample positioning limitations of conventional indentation techniques can be overcome through hybrid indenters, coupling depth-sensing indentation with piezo scanning capabilities.[31,32] With a hybrid indenter, AFM-like intermittent contact imaging using force modulation has been demonstrated.[33] More recently, we have shown that with contact force modulation using a hybrid nanoindenter, it is possible to quantitatively map the surface stiffness.[34,35] These stiffness images are produced by monitoring the tip displacement amplitude and phase responses to an applied sinusoidal force, and are properly interpreted as a complex quantity containing both elastic (storage) and dissipative (loss) components.

In this article, we present an imaging technique that we use to map the tip–sample mechanical response quantitatively using the hybrid indenter. The advantage of this approach is that not only can it be used to map the stiffness contrast *but also to map the elastic modulus quantitatively, for both storage and loss components*. The storage and loss moduli determined from the images are compared to the measurements made with conventional depth-sensing nanoindentation techniques. Issues that must be addressed in order to map the mechanical properties quantitatively, such as instrument dynamics, feedback modulation of the piezo, indenter tip shape calibration, as well as contributions of adhesion and sliding, are discussed.

II. EXPERIMENT

One of the barriers preventing quantitative mechanical property imaging in AFM or other scanning techniques is that the measured response is the convolution of the tip–sample interaction and the measuring instrument. A number of factors must be accounted for to interpret this response. For dynamic measurements, the system mechanics (mass, spring constant, and damping loss) and instrument compliance must be modeled and measured, and system electronics corrections must be made. Acquiring this information while scanning adds the need to control the system feedback response, scan rates, and time constant of the lock-in amplifier used to measure the amplitude and phase of the displacement signal. Finally, to process the data, appropriate contact mechanical models and knowledge of tip geometry are necessary. Our approach to solving these problems is described next. We demonstrate measurement of storage and loss contact stiffness during scanning in continuous contact with a sample, resulting in images that map storage and loss components of the elastic modulus.

The instrument configuration used in these experiments consists of a hybrid indenter (Triboscope–Hysitron, Inc., Minneapolis, MN) on an AFM base (Multimode with JV scanner and signal access module - Digital Instruments, Santa Barbara, CA), with added ac force modulation electronics described previously.[36] Briefly, the indenter transducer consists of a capacitive core having two fixed outer plates and a spring suspended center plate to which the indenter tip is attached. The center plate is actuated by attracting the center plate towards the fixed lower plate by electrostatic means, and the resulting displacement detected by capacitive sensing. Coupling of the transducer to the AFM scanner allows both depth-sensing indentation (with the piezo feedback turned off) and topographic imaging (using the piezo feedback). Our method of dynamic mechanical property mapping is described next.

A. Dynamic indentation: Mechanical and electronic contributions

To deconvolute the actual dynamic response of the contact in a dynamic measurement, the contributions from the various electronics (e.g., filters, etc.) and mechanical elements must be known and modeled since they will be dependent on the frequency of the measurement. This problem can be solved if the transfer functions for the electronics and mechanical elements of the transducer are known or calibrated.

In our previous work, we have shown that the dynamic mechanical response of the transducer when it is in contact with the sample can be modeled using two Kelvin–Voigt mechanical equivalents.[36] For contact stiffness, much less than the machine stiffness (at least two orders of magnitude), the machine can be assumed to be rigid and the model solved analytically.[27] In this case, the amplitude of the displacement signal is

$$X_0 = \frac{F_0}{\sqrt{(k - m\omega^2)^2 + [(C_i + C_s)\omega]^2}}, \tag{1}$$

and the phase shift between force and displacement is

$$\phi = \tan^{-1}\frac{(C_i + C_s)\omega}{k - m\omega^2}, \tag{2}$$

where X_0 is the amplitude of the displacement oscillation and ϕ is the phase shift of the displacement with respect to the exciting force, F_0 is the amplitude of the sinusoidal force, m is the indenter mass, ω is the frequency in radians, C_i is the damping coefficient of the air gap in the capacitive displacement sensor, and C_s is the damping coefficient of the contact. The combined stiffness, k, is given by

$$k = K_s + K_i, \tag{3}$$

where K_s is the tip–sample contact stiffness and K_i is the spring constant of the leaf springs that hold the indenter shaft.

The indenter spring constant K_i, mass m and damping coefficient of the air gap C_i can be obtained by fitting the amplitude and phase response of the instrument (between 10 and 300 Hz) to Eqs. (1) and (2) when it is not in contact with a sample. However, for an accurate calibration, the contribution due to the electronics must be determined. In our instrument, the electronic contributions to the dynamic response are due to low-pass filters in the force actuation and displacement sensing electronics. If the transfer functions of the electronics are known, the electronic contribution for the dynamic response can be corrected (see Appendix). Figure 1(a) shows the combined dynamic compliance of the instrument (i.e., ratio of the displacement amplitude X_0 to the force amplitude F_0 with electronic contribution directly measured from the lock-in amplifier) when it is free of contact with the sample without any correction for electronics. If we attempt to fit the response to Eqs. (1) and (2), it results in a poor fit compared to the mechanical constants obtained from quasi-static (dc) measurements.

Figure 1(b) shows the dynamic compliance after correcting for the electronic contribution using Eqs. (A1), (A3), and (A5) from the appendix. The fit for the indenter constants was K_i (133 N/m), m (276 mg), and C_i (0.0208 Ns/m); the values for K_i and m are in good agreement with quasi-static measurements. Once the contributions from the electronics are corrected, the measured system response correlated well with the Kelvin–Voight mechanical equivalent model. Figure 1(c) shows the difference between the measured phase shift response ϕ with and without electronic correction. For the electronic correction, the total phase shift due to electronics [Eqs. (A2), (A4), and (A6)] is subtracted from the phase shift measured by the lock-in amplifier.

The machine compliance was measured (using the method of Oliver and Pharr)[28] and found to be 25 m/μN. If all the aforementioned constants are known or accurately calibrated, the contact stiffness K_s and contact damping coefficient C_s can be calculated using Eqs. (1)–(3). In an indentation experiment, the contact stiffness is proportional to the projected contact area, A,

$$K_s = 2E^* \sqrt{\frac{A}{\pi}}, \qquad (4)$$

where E^* is the reduced modulus (combining tip and sample). For materials which can damp the superimposed dynamic force, K_s' is the storage component of the contact stiffness in phase with the applied force, and

$$K_s'' = \omega C_s, \qquad (5)$$

where K_s'' is the loss component of the contact stiffness out of phase with the applied force. Storage and loss moduli for polymer materials obtained by this technique[37–39] compare favorably with bulk values determined through conventional dynamic testing.

The lock-in amplifier also contributes a time constant to the measurement. The settings are usually a compromise between tolerable noise and speed of data acquisition. For ex-
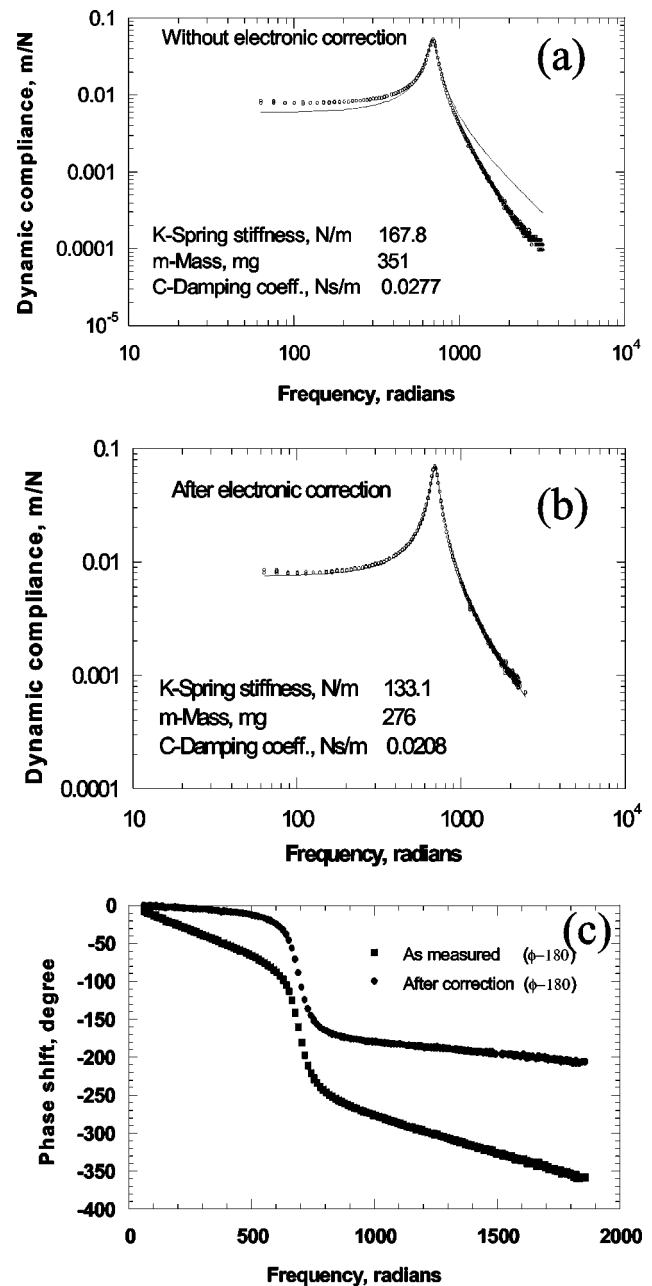

FIG. 1. Plots of dynamic compliance (amplitude ratio of X_0/F_0) of the indenter system including (a) electronic contribution and (b) after correcting for the electronic contribution are shown. The solid line is the fit for the Kelvin–Voight model. The corrected measurement follows the model prediction. (c) The phase shift as a function of frequency with and without electronic contribution.

ample, in a static measurement (i.e., at fixed load), one could optimize for the low noise in the measurement. However, both indentation and scanning operations require knowledge of the dynamic response of the indenter to the small sinusoidal force while moving the sample vertically or laterally with respect to the indenter tip. The frequency of the measurement and rate of sample movement will determine acceptable time constant settings. If the time constant setting on the lock in is too high, the data will be averaged over longer time scales than the apparent resolution of the measurement, distorting the response. In this case, a purely elas-
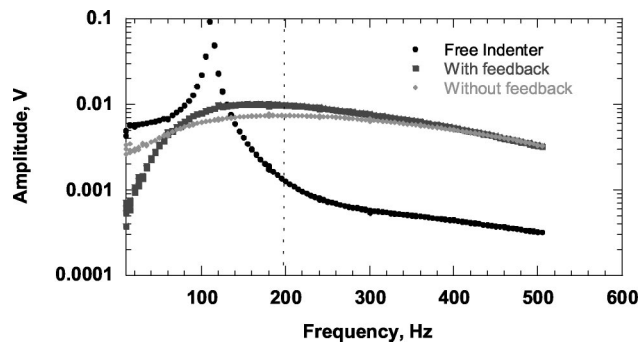
FIG. 2. The amplitude of the indenter tip response as a function of frequency for three different conditions: ● when the tip is not in contact with the surface, ■ when the tip is in contact with the surface (~1 μN load) under feedback control, and ◆ when the tip is in contact with the sample (~1 μN load) without feedback are shown.

tic deformation may appear plastic, while an image could be blurred spatially. Care must be taken to ensure that the speed of the experiment is not greater than the rate at which the lock in can detect variation in the response of the instrument.

B. Feedback issues

The use of feedback electronics during imaging presents a significant issue influencing quantitative mechanical measurements. The resonance frequency of our instrument (110 Hz) and the useable dynamic range for force modulation (10–250 Hz) are below the frequency of the feedback controller (in the kHz range) for constant load scanning. Therefore, when the tip is modulated, the feedback control will force the piezo scanner holding the sample to counter the vertical oscillation of the tip to keep constant deflection, an undesirable response. Figure 2 shows the amplitude of the indenter tip as a function of frequency for three different conditions: ● when the tip is not in contact with the surface, ■ when the tip is in contact with the surface (~1 μN load) with feedback control, and ◆ when the tip is in contact with the sample (~1 μN load) without feedback. When the tip is in contact, the resonance frequency increases (above the free resonance frequency of 110 Hz). At low frequencies, the tip displacement amplitude is lower when the tip is in feedback than without feedback. The result is an apparent ''stiffening'' of the tip–sample interaction, increasing the measured contact stiffness; this would be expected since the feedback is counteracting the tip oscillation. The higher amplitudes observed at a higher frequency with feedback on is likely due to the effects of the overall system damping. We also observe a change in phase shift under feedback control.

To overcome these problems, we have implemented an interleaved scanning technique provided with the AFM scanning software. During the first pass, the feedback control is active and the height information is stored. Then, during the next pass, the feedback is turned off and the height data collected from the first pass is used to position the Z piezo to follow the surface topography. At the same time, the tip displacement amplitude and phase data from the lock-in amplifier and the contact force data from the displacement trans-

ducer are collected. In this way, the phase and amplitude response of the contact to the sinusoidal force can be accurately measured.

C. Sample preparation

A composite made of carbon fibers (nominally 6 μm in diameter) embedded in an epoxy matrix was used for the experiments. A 2 mm thick sample was cut using a diamond saw and mechanically polished; the final polish was performed using 0.25 μm diamond paste. The sample was then mounted onto the AFM piezo scanner inside a dry box purged with dry nitrogen (RH<2%). To minimize thermal drift, the sample was allowed to equilibrate with the temperature of the dry box for at least 1 h.

D. Scanning conditions for stiffness images

Diamond indenters with tip radii between 250–600 nm were used for the experiments. The indenter tips (tip radius R and area function) were calibrated using both standard indentation techniques[28] with quartz and blind tip reconstruction[40,41] with a tip characterizer (TGT01-Silicon-MDT, Moscow, Russia). The sample was then brought into contact with the diamond tip at a constant (dc) contact force of 1.5–2 μN using AFM feedback control. To obtain the stiffness image, the indenter tip was modulated with a sinusoidal force of ~1 μN at 200 Hz, which resulted in a tip displacement amplitude between 0.5–2 nm. Interleaved scanning was performed at a scan rate of 0.1 Hz over 100 μm^2 and 512×512 pixel resolution for all the experiments. The lock-in time constant was set to 3 ms. Data were acquired and processed to obtain contact force, sinusoidal displacement amplitude and phase shift. Electronics correction factors (at 200 Hz) were 0.594 for force [see Eq. (A1)], 1.163 for displacement $(1/[(A3)*(A5)]$ and 66° for the phase shift. The data were further processed using image manipulation software (Transform, Research Systems, Boulder, CO) to obtain the damping coefficient as well as storage and loss stiffness images using Eqs. (1)–(3).

E. Indentation experiments

Both standard force-displacement[28] (to a maximum load of 200 μN) and force-modulation methods[27] were used to evaluate moduli of the various regions of the sample. Standard calibration techniques were employed to model the area function of the Berkovich tip for indents to depths greater than the tip defect.[28] The force-modulation amplitude for indents ranged between 1–3 μN at 105 Hz, with a lock-in time constant of 100 ms and indentation rate of 2–20 μN/s. Force–distance curves[42] were used to evaluate the adhesion of the indenter tip to the sample.

III. RESULTS AND DISCUSSION

A. Stiffness imaging and interpretation

Figure 3(a) shows the contact force image obtained by monitoring the indenter tip displacement using the displacement transducer and the known spring constant of the transducer. Although the contact force was kept constant around
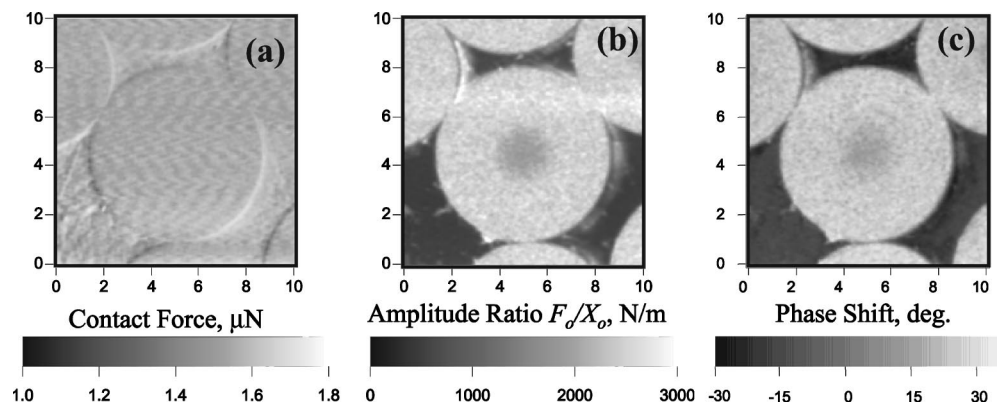
FIG. 3. Images of a carbon fiber-epoxy composite, scan size is 10 μm$\times$10 μm, for (a) the contact force (in μN), (b) the ratio of the force modulation amplitude to the displacement amplitude (in N/m and corrected for electronics, see the Appendix) corresponding to the contact force image, and (c) the true phase shift (in degrees and corrected for electronics) between the oscillating force and the displacement during scanning are shown.

1.6 μN, a small variation (100 nN) can be seen as a result of feedback error, giving slight contrast to the image. Figure 3(b) shows the ratio of the sinusoidal force amplitude F_0 to the displacement amplitude X_0 (corrected for electronics, see the Appendix) corresponding to the constant contact force imaging. The measured amplitude ratio is due primarily to the mechanical response of the sample to the applied load. Figure 3(c) shows the true phase shift (corrected for electronics) between the sinusoidal force and the displacement during scanning. From Eqs. (1) and (2), it can be observed that amplitude ratio and phase shifts can occur as a result of changes in the local damping coefficient and/or contact stiffness; contrast in the images reflects variation of the combined tip–sample elastic and damping response across the sample.

The stiffness and damping response can be deconvoluted from Figs. 3(b) and 3(c) using Eqs. (1) and (2). In this way, the images can be processed to obtain the storage and loss components of the contact stiffness using Eqs. (3) and (5). Figure 4 shows the storage and loss component of the contact stiffness. The contact stiffness is much higher for the carbon fiber than the epoxy matrix. The loss components for both are roughly 1/5 to 1/3 the storage components. The contrast in both images is now shown to be due to a variation in tip–sample interaction stiffness across the composite sample, and is similar for both the storage and loss compo-

nents. Additionally, a subtle gradient in contrast at the center of the fiber indicates that the center is more compliant than the periphery. The contrast was observed in the center of all fibers, and could be due to porosity or other nonuniformity often observed in such fibers.[43]

B. Materials property evaluation from images

The storage and loss moduli were obtained from the stiffness image by applying an appropriate contact mechanics model. For an elastic contact, in the absence of adhesion or if the applied force is much greater than the adhesion, Hertzian mechanics can be used to determine the contact radius.[44] For the present experiments, force–distance curves were used to evaluate the tip–sample adhesion. Figure 5 shows a force–distance curve (force and interaction stiffness versus sample displacement) for the carbon fiber region and a diamond indenter tip with a radius of 250 nm. The experiment was conducted at a relative humidity of ~1%. During the approach, the indenter experienced an attractive force of ~150 nN before making contact with the sample. During pull-off measurements, the adhesion was 150$\pm$30 nN. The interpretation of the force and interaction stiffness curves is given elsewhere.[35,42] For the images shown, adhesion from different regions of the sample ranged between 100–200 nN. Because the applied contact force was ~1600 nN, it is rea-
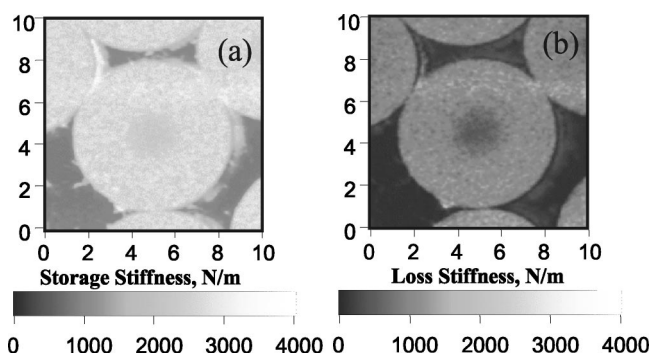

FIG. 4. Images of a carbon fiber-epoxy composite, scan size is 10 μm$\times$10 μm, for (a) the storage and (b) loss components of the contact stiffness are shown.

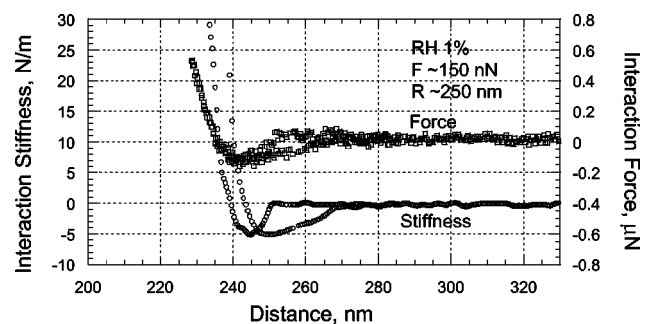FIG. 5. Force–distance curves showing the interaction stiffness between a diamond indenter tip (with a radius of 250 nm) and carbon fiber are shown.
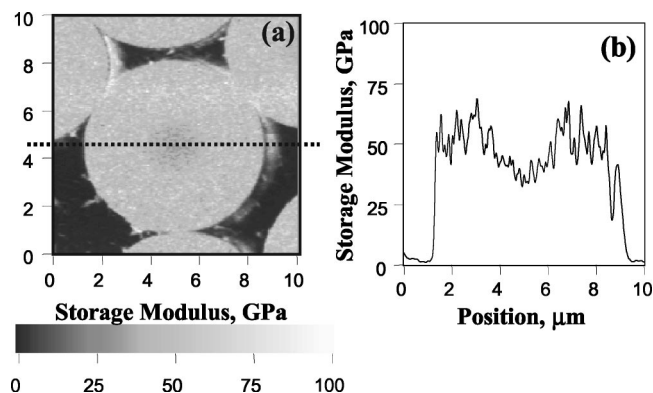
FIG. 6. (a) Map of storage modulus (in GPa) and (b) line scan of the carbon fiber-epoxy composite are shown. Scan size is 10 μm$\times$10 μm. The image contrast is due to change in elastic modulus. Line scan through the center of the image shows storage modulus gradient at the center of the fiber.

FIG. 7. (a) Map of loss modulus (in GPa) and (b) line scan of the carbon fiber-epoxy composite are shown. Scan size is 10 μm$\times$10 μm. Contrast in the image is due to change in loss modulus. Line scan through the center of the image shows loss modulus gradient at the center of the fiber.

sonable to apply Hertzian contact mechanics. In this case, for a spherical indenter in contact with a sample, the radius of the contact area, a, is

$$a = \left(\frac{3FR}{4E^*} \right)^{1/3}, \tag{6}$$

where F is the applied load and R is the radius of curvature of the tip. Equation (6) is valid for a nonsliding contact. For sliding contacts, Johnson[45,46] predicted that the contact radius may be reduced compared to static contact. However, the experimental evidence using AFM by Carpick *et al.*[47] and surface force apparatus (SFA) by Israelachvili[48] suggests that there is only very little or no change in contact area during sliding in AFM and SFA experiments, respectively. Assuming that sliding during scanning does not significantly change the contact area, Eqs. (4) and (6) can be combined to obtain the reduced modulus

$$E^* = \sqrt{\frac{K_s^3}{6FR}}. \tag{7}$$

Figures 6(a) and 7(a) show the reduced modulus images (storage and loss) calculated by substituting the contact force and stiffness data into Eq. (7). The contrast clearly shows that the modulus at the center of the fiber is less than at the periphery, while the modulus of the epoxy is at least an order of magnitude less than the fiber. Edge artifacts can be clearly distinguished from true mechanical response, but are minimal here due to a good sample polish. To reduce the noise, the data were averaged. A cross section of the data running across the center of the fiber is shown in Figs. 6(b) and 7(b). The storage modulus of the epoxy is $\sim$1.3 GPa, while the fiber center is $\sim$35 GPa, increasing slowly to a constant value of $\sim$53 GPa at the periphery. Loss moduli for both regions are about 1/5 to 1/3 that of the storage moduli.

C. Comparison with standard techniques

For comparison, conventional indentation experiments were done at different locations of the sample. Figure 8 shows the indentation response at the center (A) and periphery (B) of the fiber, and in the epoxy (C) for a maximum load
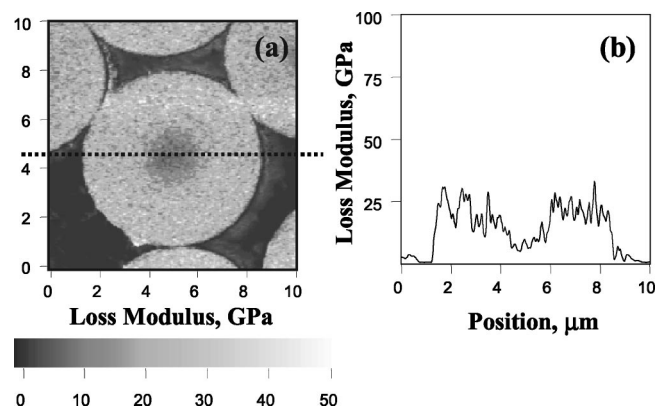
of 200 μN. The modulus calculated from load-displacement graphs using standard unloading slope analyses is 3.5$\pm$0.5 GPa for the epoxy region, 48$\pm$2 GPa for the center of the fiber, and 57$\pm$3 GPa at the periphery. This confirms a $\sim$20% difference in modulus across the fiber, which is clearly visible in the images.

A second set of indentation experiments were done to compare dynamic properties of the sample. In these experiments, storage and loss moduli were calculated from a continuous measurement of contact stiffness at a given frequency. Figure 9 shows the contact stiffness response, at a frequency of 105 Hz, as a function of load for the carbon fiber and epoxy matrix. Because during these experiments, the indents penetrate the sample to greater depths than during the contact stiffness imaging experiment, the fit for the Berkovich tip is used rather than the Hertzian approximation to calculate elastic modulus.

Figure 10 shows a comparison of modulus measurements by indentation and imaging. To get a statistical estimate of the modulus from the imaging technique, histograms of the image data were analyzed, and mean and standard deviation of moduli for the various regions were obtained by peak fits using normal distributions.

The reduced moduli calculated from the scanned images are in excellent agreement with the indentation measure-
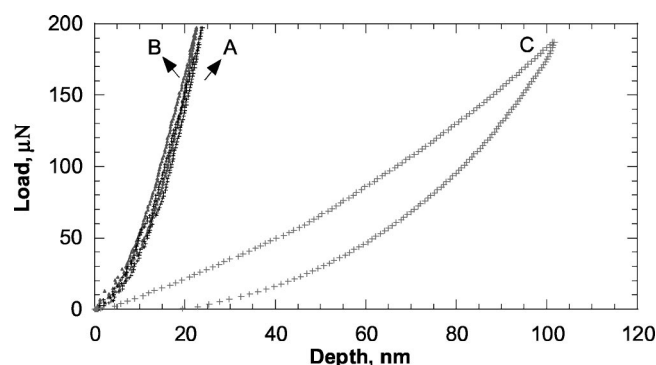

FIG. 8. Conventional load-displacement indentation curves of the carbon-epoxy composite at the center (A) and periphery (B) of the fiber and in the epoxy (C) matrix are shown. A maximum load of 200 μN was applied.
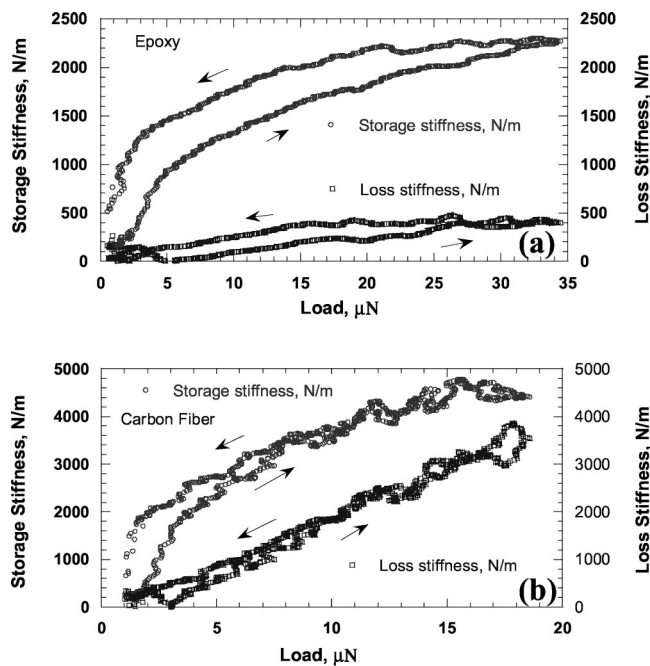
FIG. 9. Plots of the storage and loss contact stiffness (in N/m) for (a) the epoxy matrix and (b) carbon fiber as a function of load (in μN) are shown.

ments for both the storage and loss components. Some variation of modulus between the new image mode and conventional indentation mode maybe attributed to differences in the frequency response of the materials; in any case, the agreement is quite good. The larger scatter in the moduli obtained from the fiber region with the imaging technique is due to noise, which can be reduced by increasing the amplitude of the force modulation. However, imaging conditions were optimized to get a measurable displacement response from both fiber and epoxy regions. The storage moduli compare favorably to literature values[26] for other carbon fibers. The good correlation between the imaging (low load) and indentation (higher load) modes suggests that the sample polishing technique did not damage the surface, as was observed in previous low load indentation experiments on aramid fibers.[49]
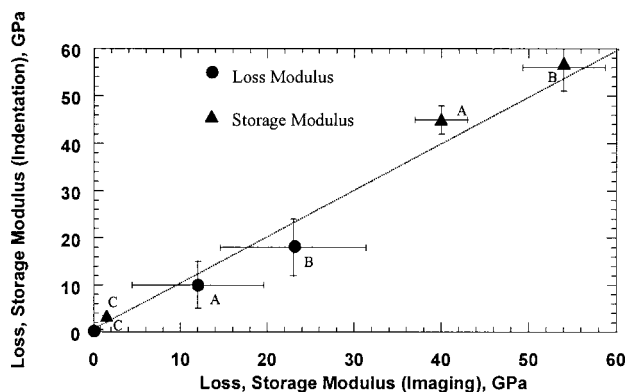

FIG. 10. Comparison of modulus measurements made by indentation and imaging at the center, (A), and periphery, (B), of the fiber and epoxy, (C) are shown.

The imaging results can improve the way we conduct mechanical property measurements in several ways. Rather than depending on topography alone in a scanned image to select indentation locations, the contrast in the phase and amplitude response can be used to identify regions of interest. This could be especially valuable in nanocomposites, polymers or tribological surfaces, for example, where topography may not correspond to mechanical property differences, or in studies of subsurface delamination of thin films. At the scan rates used in these experiments, the images take about 2–3 h to complete. While this is considerably longer than conventional scanning rates in AFM, the images can be analyzed and converted to quantitative stiffness and modulus maps in a matter of minutes. Importantly, this method eliminates the tedious task of performing and analyzing indentation arrays where sample nonuniformities (e.g., defects, asperities, and edge effects) are difficult to locate and interpret. Furthermore, because the tip–sample interaction is elastic, the spatial resolution is also improved over indentation maps, where indents should be spaced far apart to eliminate the effects of residual stress and plastic deformation from neighboring indents. Any inelastic tip–sample interactions (i.e., plastic deformation) will also limit the application of this technique; hence, experiments should be performed at the lowest practical load. The results confirm that quantitative mapping of dynamic mechanical properties, with the tip in continuous contact with the surface, is possible if proper instrument calibration and analysis are performed.

IV. CONCLUSIONS

Quantitative imaging of contact stiffness and elastic modulus (storage and loss) was demonstrated for a fiber-epoxy sample using a hybrid nanoindentation apparatus that combines depth-sensing indentation with the imaging capabilities of AFM. Good correlation of storage and loss moduli was found between imaging and measurements made using conventional nanoindentation techniques. Contrast in the phase and amplitude images, without the detailed processing employed in this article, can also be used to identify regions of interest for indentation measurements as well as aid in interpreting subtle changes in mechanical properties.

ACKNOWLEDGMENTS

APPENDIX

The transducer and its accompanying electronics have been designed to achieve a balance between maximizing signal-to-noise ratio and preserving bandwidth sufficient for quasi-static operation over a meaningful range of loading and displacement rates. In the case of dynamic operation, however, much more detailed attention must be given to filters (component transfer functions), as they affect the measured response versus frequency spectrum. Of course, not all transfer functions need be considered in terms of frequency
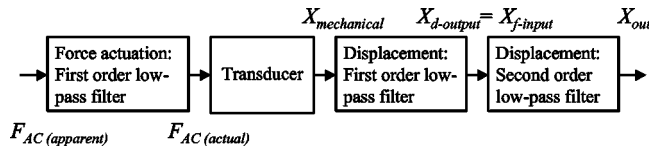
FIG. 11. Block diagram of relevant filters affecting the phase and amplitude of the ac displacement signal is shown.

dependency, rather only those that ultimately impart an unacceptable level of error to the determination of materials properties over the dynamic testing bandwidth.

Three low-pass filters relevant to the dynamic testing bandwidth used in this work exist along the signal path from the point of force actuation to the point of measuring the displacements (see Fig. 11). They are (1) a first-order filter affecting the oscillatory component of the force actuation voltage, (2) a first-order filter after the synchronous demodulator that is integral to the capacitive sensing technique, and (3) a user-selectable second-order filter operating on the demodulated and filtered displacement signal just prior to digitization by the data acquisition system. Transfer functions for these filters are described below in terms of RC time constants, resistor ratios, and frequency ω in order to illustrate their functional form. Specific component values are not given as they have evolved over the course of time, and would not be universally applicable.

1. Correcting the applied force

The force modulation electronics used in this work employ a square-root circuit to generate the voltage to be amplified and filtered by the actuation electronics, with its output given by $V_{SR} = \sqrt{V_{dc} + V_{ac} \sin \omega t}$. This circuit is appealing from the standpoint that for a parallel-plate capacitor the electrostatic force is proportional to the square of voltage, which would lead to the "clean" result of the applied dynamic force always proportional to $V_{dc} + V_{ac} \sin \omega t$.[36] The presence of the actuation filter, however, precludes straightforward application of this concept across the dynamic testing bandwidth.

Typically, the transducer is biased with a dc voltage V_{dc}, which is set approximately two orders of magnitude greater than V_{ac}; hence, evaluating the case of $V_{dc} \gg V_{ac}$ is most appropriate to this study. In this limit, the square-rooted functional form $\sqrt{V_{dc} + V_{ac} \sin \omega t}$ can be approximated by $a_0 + a_1 \sin \omega t$, where $a_0 = 0.5[\sqrt{V_{dc} + V_{ac}} + \sqrt{V_{dc} - V_{ac}}]$ and $a_1 = 0.5[\sqrt{V_{dc} + V_{ac}} - \sqrt{V_{dc} - V_{ac}}]$ if one imposes equal oscillation amplitude. For the values of V_{dc}, V_{ac} used in these experiments, this approximation deviates maximally from the true functional form by only 0.001%; the harmonic content at 2ω is nearly three orders of magnitude smaller than the fundamental. The practical implication of this exercise is that the oscillatory component of the dynamic force is limited to the fundamental, and that the frequency dependency of its amplitude is governed by the transfer function for the classical passive first-order low-pass filter acting on a sinusoidal input. In other words,

$$\left| \frac{F_{ac(actual)}}{F_{ac(apparent)}} \right| = \frac{1}{\sqrt{1 + (\omega RC)^2}}, \tag{A1}$$

with the phase lag introduced to the signal as

$$\tan \theta = \omega RC. \tag{A2}$$

Interestingly, application of the square-root circuit eliminates coupling between ac and dc components in determining the force amplitude of the ω term, which would not be the case, in general, for arbitrary a_0 and a_1. It is noted, however, that the square-rooted functional form deviates significantly from a simple dc-shifted sinusoid in the limit of V_{ac} approaching V_{dc}, therefore, the harmonic content must be considerable in this case. Consequently, knowing the resultant coefficients of the force amplitude spectrum, in the presence of the actuation filter, takes on a measure of complexity in that limit.

2. Correcting the displacement signal (step 1)

The first correction to the measured displacement X involves the transfer function of the active first-order low-pass filter acting on the output of the synchronous demodulator, which is described by

$$\left| \frac{X_{d-output}}{X_{mechanical}} \right| = \frac{1 + R_2/R_1}{\sqrt{(1 + R_2/R_1)^2 + (2\omega R_2 C)^2}}, \tag{A3}$$

and a phase lag of

$$\tan \theta = \frac{2\omega R_2 C}{1 + R_2/R_1}. \tag{A4}$$

In Eq. (A3), $X_{mechanical}$ is the actual displacement amplitude and $X_{d-output}$ is the filtered displacement amplitude after demodulation.

3. Correcting the displacement signal (step 2)

The second and final correction to the measured displacement involves the transfer function for the user-selectable active second-order low-pass filter just prior to the point of digitization, which is described by

$$\left| \frac{X_{output}}{X_{f-input}} \right| = \frac{1}{\sqrt{A^2 + B^2}}, \tag{A5}$$

where $X_{f-input} = X_{d-output}$ from Eq. (A3), $A = 1 - \omega^2 R_1 C_1 R_2 C_2$ and $B = \omega C_2 (R_1 + 2R_2)$, with the phase lag given by

$$\tan \theta = \frac{B}{A}. \tag{A6}$$

In summary, the force amplitude is governed by Eq. (A1), the mechanical displacement amplitude can be found by dividing the measured displacement amplitude by Eqs. (A3) and (A5), and the mechanical phase shift corresponds to the phase shift measured relative to the square-root circuit output minus the sum of electronic phase shift (phase lag) given by Eqs. (A2), (A4), and (A6).

D. Alternative (simplified) phase shift correction method

An alternative method to correct for phase shift due to electronics can be accomplished by zeroing the phase at the lock-in amplifier for a given (fixed) driving frequency. In this case, it is necessary to know the dynamics of the transducer when it is free of contact.[27] The corrected phase shift ϕ_c in this case is

$$\phi_c = \tan^{-1}\left(\frac{\omega C_i}{K_i - m\omega^2}\right) + \theta, \tag{A7}$$

where C_i is the damping coefficient of the transducer, K_i is the spring stiffness, m is the mass of the transducer, and θ is the measured phase shift from the lock-in after zeroing the phase manually on the lock-in. In the present experiment, the phase shift due to electronics is 66° at a driving frequency of 200 Hz.

[1] H. Engqvist and U. Wiklund, Tribol. Lett. **8**, 147 (2000).

[2] D. W. Moon, R. W. Fonda, and G. Spanos, Weld. J. (Miami) **79**, 278S (2000).

[3] K. O. van der Werf, C. A. J. Putman, B. G. de Grooth, and J. Greve, Appl. Phys. Lett. **65**, 1195 (1994).

[4] M. Radmacher, J. P. Cleveland, M. Fritz, H. G. Hansma, and P. K. Hansma, Biophys. J. **66**, 2159 (1994).

[5] D. D. Koleske, G. U. Lee, B. I. Gans, K. P. Lee, D. P. DiLella, K. J. Wahl, W. R. Barger, L. J. Whitman, and R. J. Colton, Rev. Sci. Instrum. **66**, 1 (1995).

[6] M. Heuberger, G. Dietler, and L. Schlapbach, Nanotechnology **6**, 12 (1995).

[7] V. V. Tsukruk and Z. Huang, Polymer **41**, 5541 (2000).

[8] S. M. Hues, C. F. Draper, K. P. Lee, and R. J. Colton, Rev. Sci. Instrum. **65**, 1561 (1994).

[9] M. R. VanLandingham, J. S. Villarubia, W. F. Guthrie, and G. F. Meyers, in *Nanoindentation of Polymers: An Overview*, Macromolecular Symposia, Vol. 167, Mar. 2001 (Wiley, Berlin, 2001), pp. 15–43.

[10] M. R. VanLandingham, S. H. McKnight, G. R. Palmese, J. R. Elings, X. Huang, T. A. Bogetti, R. F. Eduljee, and J. W. Gillespie, J. Adhes. **64**, 31 (1997).

[11] P. Maivald, H. J. Butt, S. A. Gould, C. B. Prater, B. Drake, J. A. Gurley, V. B. Elings, and P. K. Hansma, Nanotechnology **2**, 103 (1991).

[12] K. Yamanaka, H. Ogiso, and O. Kolosov, Appl. Phys. Lett. **64**, 178 (1994).

[13] T. Kajiyama, K. Tanaka, I. Ohki, S. R. Ge, J. S. Yoon, and A. Takahara, Macromolecules **27**, 7932 (1994).

[14] N. A. Burnham, A. J. Kulik, G. Gremaud, P. J. Gallo, and F. Oulevey, J. Vac. Sci. Technol. B **14**, 794 (1996).

[15] F. Oulevey, G. Gremaud, A. Semoroz, A. J. Kulik, N. A. Burnham, E. Dupas, and D. Gourdon, Rev. Sci. Instrum. **69**, 2085 (1998).

[16] A. Rosa, E. Weilandt, S. Hild, and O. Marti, Meas. Sci. Technol. **8**, 1333 (1997).

[17] U. Rabe, V. Scherer, S. Hirsekorn, and W. Arnold, J. Vac. Sci. Technol. B **15**, 1506 (1997).

[18] N. A. Burnham, G. Gremaud, A. J. Kulik, P.-J. Gallo, and F. Oulevey, J. Vac. Sci. Technol. B **14**, 1308 (1996).

[19] J. Tamayo and R. Garcia, Appl. Phys. Lett. **71**, 2394 (1997).

[20] J. Tamayo and R. Garcia, Appl. Phys. Lett. **73**, 2926 (1998).

[21] O. P. Behrend, L. Odoni, J. L. Loubet, and N. A. Burnham, Appl. Phys. Lett. **75**, 2551 (1999).

[22] N. A. Burnham, O. P. Behrend, F. Oulevey, G. Gremaud, P.-J. Gallo, D. Gourdon, E. Dupas, A. J. Kulik, H. M. Pollock, and G. A. D. Briggs, Nanotechnology **8**, 67 (1997).

[23] N. A. Burnham, A. J. Kulik, F. Oulevey, C. Mayencourt, D. Gourdon, E. Dupas, and G. Gremaud, in *Micro/Nanotribology and its Applications*, edited by B. Bhushan (Kluwer, Dordrecht, 1997), Vol. E330, pp. 439–454.

[24] J. Colchero, M. Luna, and A. M. Baro, Appl. Phys. Lett. **68**, 2896 (1996).

[25] S. Ge, Y. Pu, W. Zhang, M. Rafailovich, J. Sokolov, C. Buenviaje, R. Buckmaster, and R. M. Overney, Phys. Rev. Lett. **85**, 2340 (2000).

[26] P. E. Mazeran and J. L. Loubet, Tribol. Lett. **7**, 199 (1999).

[27] J. B. Pethica and W. C. Oliver, Physica Scripta **T19A**, 61 (1987).

[28] W. C. Oliver and G. M. Pharr, J. Mater. Res. **7**, 1564 (1992).

[29] S. P. Jarvis, A. Oral, T. P. Weihs, and J. B. Pethica, Rev. Sci. Instrum. **64**, 3515 (1993).

[30] E. L. Florin, M. Radmacher, B. Fleck, and H. E. Gaub, Rev. Sci. Instrum. **65**, 639 (1994).

[31] S. A. Joyce and J. E. Houston, Rev. Sci. Instrum. **62**, 710 (1991).

[32] B. Bhushan, A. V. Kulkarni, W. Bonin, and J. T. Wyrobek, Philos. Mag. A **74**, 1117 (1996).

[33] O. L. Warren, J. F. Graham, and P. R. Norton, Rev. Sci. Instrum. **68**, 4124 (1997).

[34] S. A. Syed Asif, K. J. Wahl, and R. J. Colton, in *Thin Films—Stresses and Mechanical Properties VIII*, edited by R. Vinci, O. Kraft, N. Moody, P. Besser, and E. Shaffer II (Materials Research Society, Pittsburgh, 2000), Vol. 594, pp. 471–476.

[35] S. A. Syed Asif, R. J. Colton, and K. J. Wahl, in *Interfacial Properties on the Submicron Scale*, edited by J. E. Frommer and R. M. Overney (American Chemical Society, Washington, DC, 2001), Vol. 781, pp. 198–215.

[36] S. A. Syed Asif, K. J. Wahl, and R. J. Colton, Rev. Sci. Instrum. **70**, 2408 (1999).

[37] S. A.Syed Asif, Thesis, (Oxford University Press, London, 1997).

[38] S. A. Syed Asif and J. B. Pethica, in *Thin-Films — Stresses and Mechanical Properties VII*, edited by R. C. Cammarata, E. P. Busso, M. Nastasi, and W. C. Oliver (Materials Research Society, Pittsburgh, 1998), Vol. 505, pp. 103–108.

[39] J. L. Loubet, W. C. Oliver, and B. N. Lucas, J. Mater. Res. **15**, 1195 (2000).

[40] J. S. Villarrubia, Surf. Sci. **321**, 287 (1994).

[41] J. S. Villarrubia, J. Vac. Sci. Technol. B **14**, 1518 (1996).

[42] S. A. Syed Asif, K. J. Wahl, and R. J. Colton, J. Mater. Res. **15**, 546 (2000).

[43] J.-B. Donnet and R. C. Bansal, *Carbon Fibers* (Marcel Dekker, New York, 1990).

[44] K. L. Johnson, *Contact Mechanics* (Cambridge University Press, Cambridge, UK, 1985).

[45] K. L. Johnson, in *Micro/Nanotribology and Its Applications*, edited by B. Bhushan (Kluwer, Dordrecht, 1997), Vol. 330, pp. 151–168.

[46] K. L. Johnson, Proc. R. Soc. London, Ser. A **453**, 163 (1997).

[47] R. W. Carpick, N. Agrait, D. F. Ogletree, and M. Salmeron, Langmuir **12**, 3334 (1996).

[48] J. N. Israelachvili, in *Fundamentals of Friction: Macroscopic and Microscopic Processes*, edited by I. L. Singer and H. M. Pollock (Kluwer, Dordrecht, 1992), Vol. 220, pp. 351–385.

[49] J. F. Graham, C. McCague, O. L. Warren, and P. R. Norton, Polymer **41**, 4761 (2000).